

Article

# Tribological Behavior of Boronized Fe<sub>40</sub>Mn<sub>20</sub>Cr<sub>20</sub>Ni<sub>20</sub> High-Entropy Alloys

Xin Guo, Xi Jin, Xiaohui Shi, Huijun Yang \*, Min Zhang and Junwei Qiao \*

College of Materials Science and Engineering, Taiyuan University of Technology, Taiyuan 030024, China; guoxin0136@link.tyut.edu.cn (X.G.); jinxi@tyut.edu.cn (X.J.); sxhtough@126.com (X.S.); zm-821202@163.com (M.Z.)

\* Correspondence: pineyang@126.com (H.Y.); qiaojunwei@gmail.com (J.Q.)

**Abstract:** The tribological behavior of hot-rolled and boronized Fe<sub>40</sub>Mn<sub>20</sub>Cr<sub>20</sub>Ni<sub>20</sub> high-entropy alloys (HEAs) sliding against a Si<sub>3</sub>N<sub>4</sub> ball was investigated in the air, deionized water and seawater. The results showed that the hot-rolled Fe<sub>40</sub>Mn<sub>20</sub>Cr<sub>20</sub>Ni<sub>20</sub> HEA was composed of an FCC (face-centered cubic) phase. In addition, the boronized HEA was composed of a great number of borides, including CrB, FeB, MnB, Fe<sub>2</sub>B, Fe<sub>3</sub>B and MnB<sub>2</sub>. The hardness increased from 139 HV to 970 HV after boronizing. In air, the wear rate decreased from  $4.51 \times 10^{-4}$  mm<sup>3</sup>/Nm to  $0.72 \times 10^{-4}$  mm<sup>3</sup>/Nm after boronizing. The wear mechanism transformed from abrasive wear and oxidative wear to the polishing effect. After boronizing, in the deionized water, the wear rate decreased from  $1.27 \times 10^{-4}$  mm<sup>3</sup>/Nm to  $8.43 \times 10^{-5}$  mm<sup>3</sup>/Nm. The wear mechanism transformed from abrasive wear and delamination wear to delamination wear. In the seawater, the wear rate decreased by about ten times that of hot-rolled alloy.

**Keywords:** high-entropy alloys; boronized; wear; oxidation; lubricate



**Citation:** Guo, X.; Jin, X.; Shi, X.; Yang, H.; Zhang, M.; Qiao, J. Tribological Behavior of Boronized Fe<sub>40</sub>Mn<sub>20</sub>Cr<sub>20</sub>Ni<sub>20</sub> High-Entropy Alloys. *Metals* **2021**, *11*, 1561. <https://doi.org/10.3390/met11101561>

Academic Editor:  
Alexander Kauffmann

Received: 12 August 2021  
Accepted: 27 September 2021  
Published: 29 September 2021

**Publisher's Note:** MDPI stays neutral with regard to jurisdictional claims in published maps and institutional affiliations.



**Copyright:** © 2021 by the authors. Licensee MDPI, Basel, Switzerland. This article is an open access article distributed under the terms and conditions of the Creative Commons Attribution (CC BY) license (<https://creativecommons.org/licenses/by/4.0/>).

## 1. Introduction

Since the concept of high-entropy alloy (HEA) [1] was proposed, it has attracted much attention. The design concept of HEAs is very different from that of conventional alloys. One element is used as the principal element in traditional alloys, whose mechanical performances are improved by adding other minor elements. Different from traditional alloys, HEAs contain five or more principal elements, and the concentration of each principal element is between 5 at.% and 35 at.% [2–5]. This kind of alloy tends to form simple solid solutions rather than complex intermetallic compounds, which is mainly attributed to the high-entropy effect, such as face-centered cubic (FCC), body-centered cubic (BCC) or hexagonal close-packed (HCP) solid solutions [6–9]. Therefore, HEAs possess a great number of excellent performances, such as high strength and hardness and excellent corrosion resistance and wear resistance as well as improved damage tolerances [3,10–15]. At present, HEAs have the potential to be the next-generation structural alloys.

In practical applications, part of the failure of metallic materials is caused by wear [16]. Therefore, improving the wear resistance of materials is an urgent problem to be solved. At present, surface modification, such as carburizing [17], nitriding [18] and boronizing [19], has been successfully applied to improve the surface properties of many kinds of metals and alloys. The abrasive wear resistance of the brittle carburized layer (0.8–2 mm) is low due to its high thickness after carburizing, and subsequent heat treatments are usually employed to obtain higher wear resistance. However, the thickness of the nitriding layer is low (<20 μm), and the preparation process is long (9–40 h). Boronizing is a thermochemical and surface hardening process. The boride layer can be formed on the surface, which greatly improves the surface hardness of materials. Moreover, boronizing technology possesses simple operation and low cost and has been successfully applied to steels, nickel-based alloys and titanium alloys etc. [17,20,21]. Tabur et al. [22] used solid-state

boronizing technology to boronize AISI 8620 steels. It was found that the microhardness value exceeded 1600 HV after boronizing, and the boronized steel revealed a 500% improvement in wear resistance. Recently, boronizing technology has also been successfully applied to the field of HEAs. Hou et al. [23] studied the effect of boronizing on the surface strengthening of  $\text{Al}_{0.25}\text{CoCrFeNi}$  HEAs. The boronized alloy had a hardness of 1136 HV, which was six times higher than that of the unboronized alloys. Additionally, the wear rate was  $1.25 \times 10^{-5} \text{ mm}^3/\text{Nm}$ , which was reduced by 12 times compared with that of the sample without boronizing. Wu et al. [24] studied the effect of boronizing time on the wear resistance of  $\text{Al}_{0.1}\text{CoCrFeNi}$  HEAs. The results showed that the wear rate under dry conditions decreased from  $1.02 \times 10^{-4} \text{ mm}^3/\text{Nm}$  to  $0.55 \times 10^{-4} \text{ mm}^3/\text{Nm}$  as the boronization time increased from 2 h to 8 h. The main wear mechanism changed from delamination wear of the boronized samples at 2 h to the polishing effect of the boronized alloys at 8 h.

$\text{CoCrFeMnNi}$  HEAs contain a large amount of expensive Co element, and it is urgent to develop Co-free HEAs with high mechanical performances. Bian et al. [25] first reported a Co-free  $\text{Fe}_{40}\text{Mn}_{20}\text{Cr}_{20}\text{Ni}_{20}$  HEA. It indicated that the ultimate yield strength and tensile strength at 77 K could reach 1.2 GPa and 1.34 GPa, respectively, and the uniform elongation was 22% due to the accumulation and entanglement of a large number of dislocations and the activation of deformation twins at low temperatures. Nutor et al. [26] found that the  $\text{Fe}_{50}\text{Mn}_{27}\text{Cr}_{13}\text{Ni}_{10}$  alloy had a tensile strength of 463 MPa and an elongation of over 40% after thermomechanical treatment, which was comparable to that of other expensive high-temperature alloys. The above newly developed Co-free HEAs with low costs will be popular in the field of structural alloys in the future. To date, there are only a few studies on the tribological behavior of these kinds of alloys for actual engineering applications. In this study, the tribological behavior of hot-rolled and boronized  $\text{Fe}_{40}\text{Mn}_{20}\text{Cr}_{20}\text{Ni}_{20}$  HEAs in dry, deionized water and seawater was discussed in detail.

## 2. Materials and Methods

### 2.1. Materials Preparation

Alloy ingots with a nominal composition of  $\text{Fe}_{40}\text{Mn}_{20}\text{Cr}_{20}\text{Ni}_{20}$  were prepared by vacuum induction melting and hot rolled at 1150 °C after homogenization at 1300 °C for 1.5 h. After hot rolling, the thickness of the sample was reduced by 79%. The purity of the initial elements was 99.95%. The purpose of hot rolling was to destroy the casting organization of the ingot, refine the grain of the alloy and eliminate microstructural defects. Therefore, a denser alloy was obtained, and the mechanical properties were improved. The hot-rolled alloy was sliced into small specimens with a dimension of 80 mm × 10 mm × 2 mm by an electro-spark wire-electrode cutting machine, then ground and well-polished. The boronizing agent (LSB-IIA,  $\text{B}_4\text{C}$ ,  $\text{KBF}_4$  and  $\text{SiC}$ ) was put into a stainless steel box and heated at 100 °C for 1 h in a resistance furnace before boronizing to get rid of the moisture in the boronizing agent. Then, the samples were put into the center of the stainless steel box and surrounded by the boronizing agent. Subsequently, the stainless steel box was sealed with clay and  $\text{Na}_2\text{O} \cdot n\text{SiO}_2$ . Then, the box was put into a heat treatment furnace at 900 °C for 6 h. The final sample was cooled with the furnace. The hot-rolled and boronized alloys were sliced into small specimens with a dimension of 10 mm × 5 mm × 2 mm by an electro-spark wire-electrode cutting machine for subsequent wear experiments.

### 2.2. Friction and Wear Test

A ball-on-block high-speed reciprocating wear test apparatus (MFT-R4000, Lanzhou, China) was used for the friction and wear testing. The tested samples were rubbed against a hardened  $\text{Si}_3\text{N}_4$  ball with a diameter of 5 mm. The hardness of the  $\text{Si}_3\text{N}_4$  ball was above 1500 HV. The wear experiments were carried out under air, simulated seawater (3.5 wt.% NaCl) and deionized water. The sliding speed was 0.2 m/s with different loads of 5 N, 10 N and 15 N. The reciprocating amplitude and sliding time were fixed to 5 mm and 1800 s,

respectively. To ensure the reproducibility of the experiments, each group of experiments was performed at least three times.

### 2.3. Mechanical Characterization

The hardness value of the sample surface was measured using the HV-1000A micro Vickers hardness tester with a load of 500 gf for 15 s. The crystal structure of the hot-rolled samples and the boronized samples was characterized using an X-ray diffractometer (XRD, PANalytical, AERIS, Netherlands) with Co  $K_{\alpha}$  radiation. The scanning range was from  $20^{\circ}$  to  $100^{\circ}$  in  $2\theta$ . The samples were ground and polished according to the standard metallographic techniques. The mixed solution of  $FeCl_3$  and  $HCl$  was utilized as the etchant to etch the sample. A scanning electron microscope (SEM, Phenom XL SEM, Shanghai, China) equipped with an X-ray energy dispersive spectrometer (EDS) was used to analyze the microstructure, chemical composition, coating thickness, worn surface and worn debris of the hot-rolled samples and boronized samples. An X-ray photoelectron spectroscopy analysis (XPS, Thermo Scientific K-Alpha+, Waltham, MA, USA) was used to determine the chemical compounds of the wear surface. The volume loss of the alloys was calculated by measuring the depth and width of the wear scars with a 3D surface profiler. The wear volume loss is defined by

$$\Delta V = Lh(3h^2 + 4b^2)/6b \quad (1)$$

where  $\Delta V$  is the volumetric loss,  $L$  is the perimeter of the wear ring, and  $h$  and  $b$  are the depth and width of the wear scars, respectively.

The wear rate is defined as follows:

$$W_r = \Delta V / SP \quad (2)$$

where  $W_r$  is the wear rate,  $S$  is the sliding distance, and  $P$  is the load.

## 3. Results and Discussion

### 3.1. Microstructures

The microstructure of the hot-rolled  $Fe_{40}Mn_{20}Cr_{20}Ni_{20}$  HEAs is shown in Figure 1a. The alloy ingot underwent a dynamic recrystallization process during the hot rolling process. Therefore, the alloy contained equiaxed grain. The XRD pattern of the hot-rolled  $Fe_{40}Mn_{20}Cr_{20}Ni_{20}$  HEAs is illustrated in Figure 1b. It can be observed that all the diffraction peaks of the hot-rolled  $Fe_{40}Mn_{20}Cr_{20}Ni_{20}$  alloy are a single FCC solid solution, and no intermetallic compounds formed. The simple single-phase structure can be ascribed to the high-entropy effect, which is conducive to the formation of simple solid solutions rather than complex intermetallic compounds.

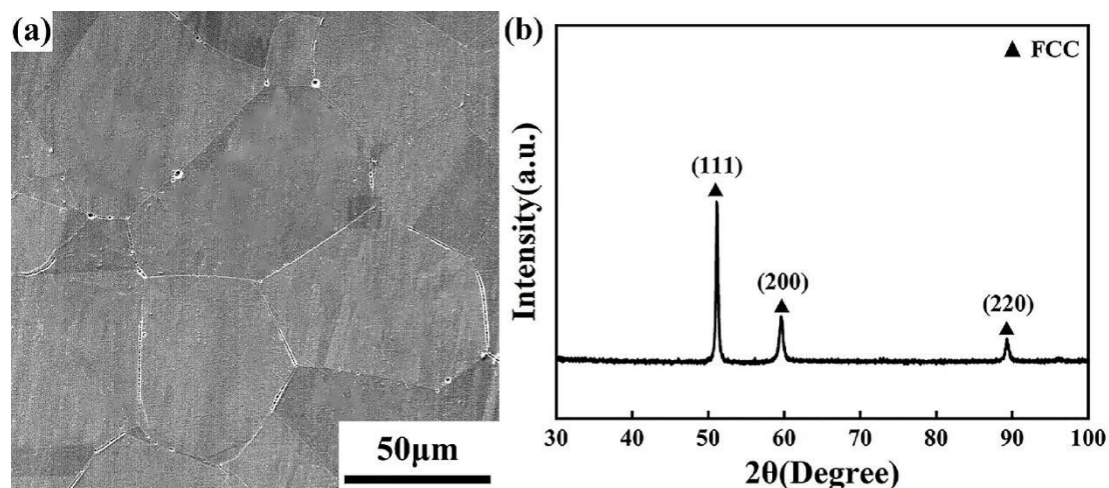


**Figure 1.** (a) Microstructures of the hot-rolled  $Fe_{40}Mn_{20}Cr_{20}Ni_{20}$  alloy and (b) XRD pattern of hot-rolled alloy.

Figure 2 shows the cross-sectional microstructure of the boronized  $\text{Fe}_{40}\text{Mn}_{20}\text{Cr}_{20}\text{Ni}_{20}$  HEA, indicating a layered structure. A dense and smooth boronized layer can be observed in the cross-sectional graph. The interface is composed of a boride layer, diffusion layer and matrix based on previous studies [24]. There is no clear demarcation line between the matrix and the boronized layer. Grain boundary precipitations within the matrix are observed. It was indicated that the boron atoms diffused through the grain boundaries and formed the precipitates at the grain boundaries. Furthermore, some cracks appear in the boride layer due to the distinctive thermal expansion coefficients of  $\text{Fe}_2\text{B}$  and  $\text{FeB}$  [27,28]. According to the EDS surface analysis results, the surface of the boronized layer is Ni rich, which can be confirmed with the XRD results. Ni-B compounds are divided into two types, one with less  $\text{BNi}_3$  and the other with more  $\text{Ni}_4\text{B}_3$ . Therefore, the sum of these two compounds leads to a higher Ni content. It is well-known that the thickness of the boride layer depends on the boronizing time and temperature. In the present study, the thickness of the boride layer was  $50.2\ \mu\text{m}$ . The element distribution diagram of the cross-section of the boronized  $\text{Fe}_{40}\text{Mn}_{20}\text{Cr}_{20}\text{Ni}_{20}$  HEA is displayed in Figure 3. The content of boron on the surface is relatively higher and gradually decreases from the surface to the substrate. This is because borides are more easily formed on the surface. The metal elements also show the characteristics of layering. The outermost layer is rich in Ni element, followed by Fe, Cr and Mn. The stratification of the metal elements is due to the different mixing enthalpies with the B element and each metal element.

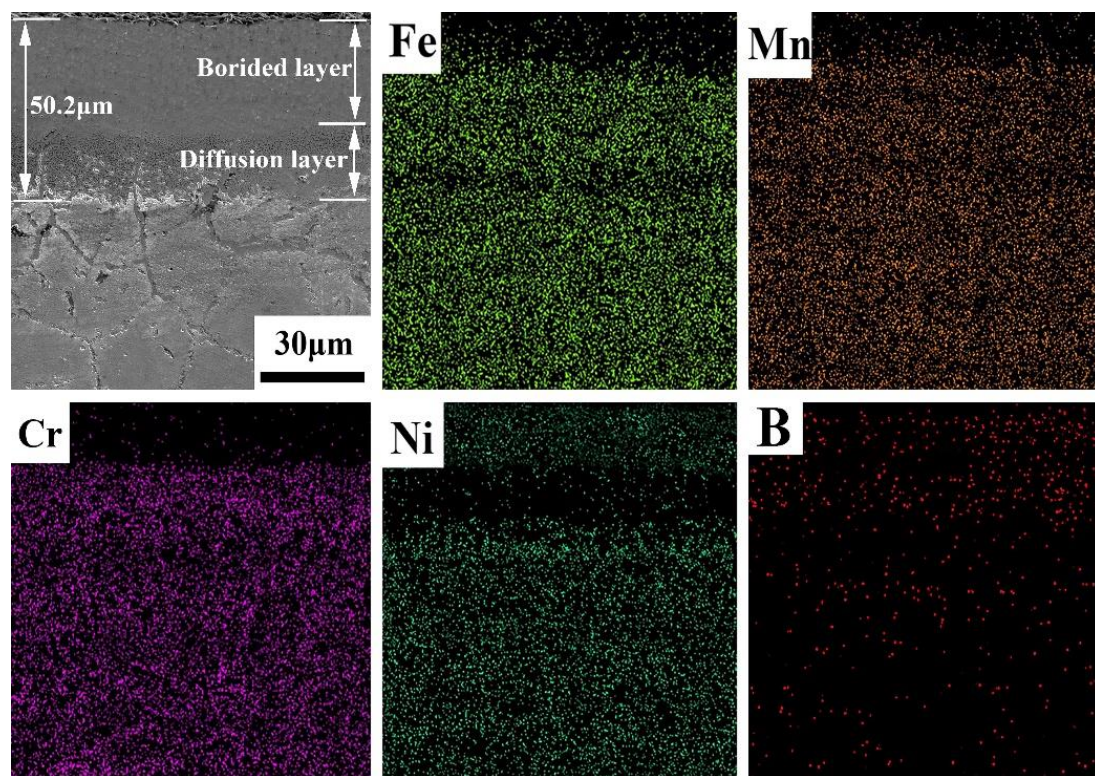


**Figure 2.** Cross-sectional SEM of the boronized  $\text{Fe}_{40}\text{Mn}_{20}\text{Cr}_{20}\text{Ni}_{20}$  alloy and EDS mapping of the boronized  $\text{Fe}_{40}\text{Mn}_{20}\text{Cr}_{20}\text{Ni}_{20}$  alloy.

Figure 3 shows the XRD pattern of the boronized HEA. Unlike that of the hot-rolled sample, no FCC structure is detected in the boronized alloy, indicating that the boron and metal elements formed a stable boride layer. It can be observed that the boronized layer mainly displays strong Cr-B and Fe-B phase-diffraction peaks. The boronized layer contains CrB, FeB, MnB,  $\text{Fe}_2\text{B}$ ,  $\text{Fe}_3\text{B}$ ,  $\text{MnB}_2$ ,  $\text{BNi}_3$ ,  $\text{Cr}_5\text{B}_3$ ,  $\text{Cr}_2\text{B}_3$ ,  $\text{Ni}_4\text{B}_3$  and other compounds. According to previous studies, the formation mechanism of the boronized layer is as follows [29]: firstly, at the boronizing temperature, boron atoms are transferred to the

surface of the materials through gas diffusion and then solid-state diffusion to the sub-surface area; secondly, as the temperature rises, the boron atoms form metal borides with the most active elements; thirdly, the boride layer consists of an outermost boride layer and an intermediate diffusion layer.

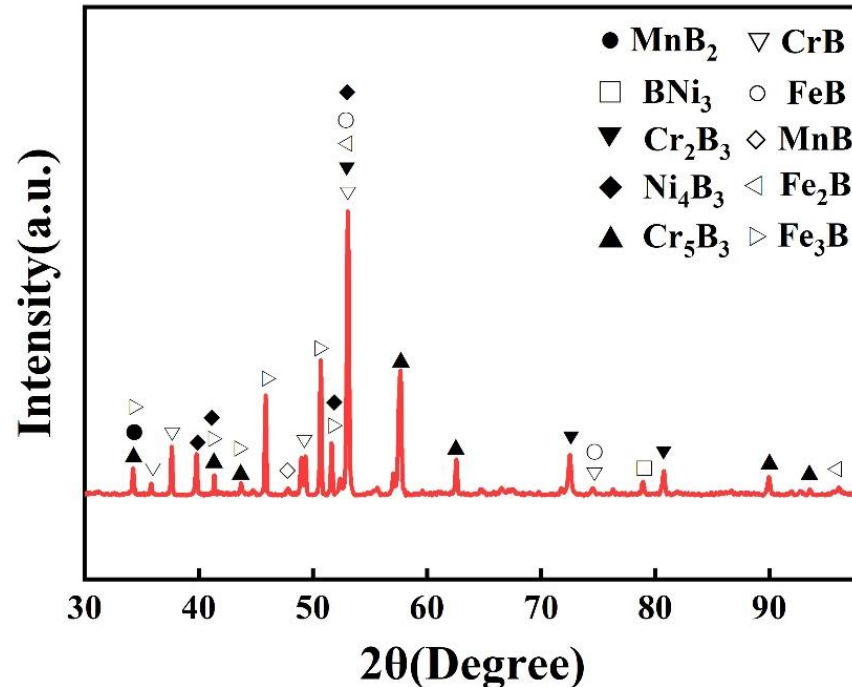


Figure 3. XRD pattern of the boronized  $\text{Fe}_{40}\text{Mn}_{20}\text{Cr}_{20}\text{Ni}_{20}$  alloy.

### 3.2. Microhardness

The hardness of the hot-rolled sample was  $139 \pm 2.7$  HV. Additionally, the hardness of the boronized sample was  $970 \pm 38$  HV, which was about 7 times higher than that of the unboronized samples owing to the presence of a large number of hard borides on the surface as shown in the XRD patterns. Moreover, the boron atoms had small atomic radii, and they were easily dissolved in the interstitial sites of the alloys, forming a supersaturated solid solution and leading to enhanced solid solution strengthening [30,31].

### 3.3. Wear Behavior

#### 3.3.1. Wear Rate

The wear rate of the hot-rolled and boronized  $\text{Fe}_{40}\text{Mn}_{20}\text{Cr}_{20}\text{Ni}_{20}$  HEAs with different loads in different environments is displayed in Figure 4. Table 1 shows the wear rate value of the hot-rolled and boronized samples. According to Archard's law [32], the wear resistance of a material is proportional to its hardness. Therefore, the wear rate of boronized alloys is lower than that of hot-rolled alloys due to the higher hardness of boronized alloys; boronized alloys have better wear resistance. In air, the wear rate of the hot-rolled alloys increased with an increase in the load. Nevertheless, the wear rate of the boronized alloys is first increased and then decreased with an increase in the load. Due to the lower hardness of the hot-rolled samples, the plastic deformation of the wear surface becomes more serious as the load increases. Additionally, the boronized alloy had higher hardness and resisted the indentation of  $\text{Si}_3\text{N}_4$  more effectively, producing less plastic deformation and leading to a lower wear rate.

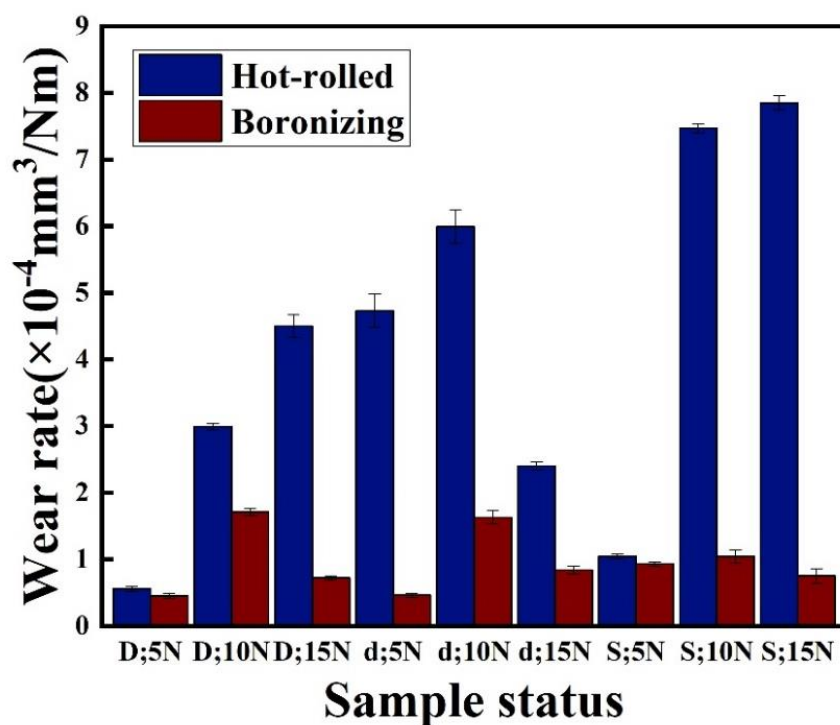


**Figure 4.** Wear rates of hot-rolled and boronized  $\text{Fe}_{40}\text{Mn}_{20}\text{Cr}_{20}\text{Ni}_{20}$  HEAs under different test environments. D symbolizes the dry condition; d symbolizes the deionized water; and S symbolizes the seawater.

**Table 1.** Average wear rate ( $\times 10^{-4} \text{ mm}^3/\text{Nm}$ ) of hot-rolled and boronized  $\text{Fe}_{40}\text{Mn}_{20}\text{Cr}_{20}\text{Ni}_{20}$  HEAs under different conditions.

Average Wear Rate ( $\times 10^{-4} \text{ mm}^3/\text{Nm}$ )	Air			Deionized Water			Seawater		
	5 N	10 N	15 N	5 N	10 N	15 N	5 N	10 N	15 N
Hot rolled	0.56	2.99	4.51	4.73	5.99	2.4	1.04	7.47	7.85
Boronized	0.45	1.71	0.72	0.46	1.63	0.84	0.93	1.04	0.75

The wear rate of both alloys is first increased and then reduced with an increase in the load in the deionized water. Moreover, the wear rate of the hot-rolled samples in the deionized water is higher than that of the dry condition. The friction heat generated by sliding oxidized the worn surface to form a dense oxide film in air, resulting in a low wear rate. The deionized water has a cooling effect, reducing the frictional heat generated on the worn surface. Therefore, the dense oxidized film cannot be easily generated on the worn surface, leading to a higher wear rate.

In the seawater, the total mass loss of the alloy can be described by Formula (3) in the corrosive environment [33].

$$m_{\text{total}} = m_{\text{ech}} + m_{\text{corr}} + m_{\text{syn}} \quad (3)$$

where  $m_{\text{ech}}$  is the mass loss caused by the dry grinding,  $m_{\text{corr}}$  is the mass loss caused by the corrosion, and  $m_{\text{syn}}$  is the mass loss caused by the synergistic effect of both corrosion and wear. On the one hand, corrosion can accelerate wear. When the metal surface is damaged by the corrosive solution, the exposed new surface is worn due to the friction force, causing additional wear. On the other hand, wear can accelerate corrosion. Abrasion destroys the passivation film and accelerates the corrosion of the materials. In the seawater, the wear rate of the hot-rolled samples gradually increased with an increase in the load. The occurrence of corrosion will cause the formation of a rough and loose corrosion product

film on the surface of the materials; their shear strength decreases, and their wear rate increases. The wear rate of the boronized alloys first increases and then decreases with an increase in the load. Furthermore, the wear rate of the boronized alloy substantially decreases.

In summary, the wear rate of the hot-rolled alloy in the dry condition is lower than that in the lubricating condition due to the oxide film formed on the wear surface. The deionized water and seawater cut off the oxygen, leading to less oxide films and a higher wear rate. However, regardless of the environment, the wear rate of the boronized alloys is lower than that of the hot-rolled alloy. The reason for the low wear rate of the boronized alloy is discussed in Section 3.4.

### 3.3.2. Friction Coefficient

The variation of the friction coefficient in the hot-rolled and boronized  $\text{Fe}_{40}\text{Mn}_{20}\text{Cr}_{20}\text{Ni}_{20}$  HEAs with the sliding time at distinctive loads under different environments is displayed in Figure 5. The specific values are summarized in Table 2. The friction coefficient curve can basically be divided into two stages: at the beginning of wear, the friction coefficient increases with time and then reaches a relatively stable value, which is called the running-in period; finally, the friction coefficient fluctuates up and down within a stable range, which is called the stable stage [34].

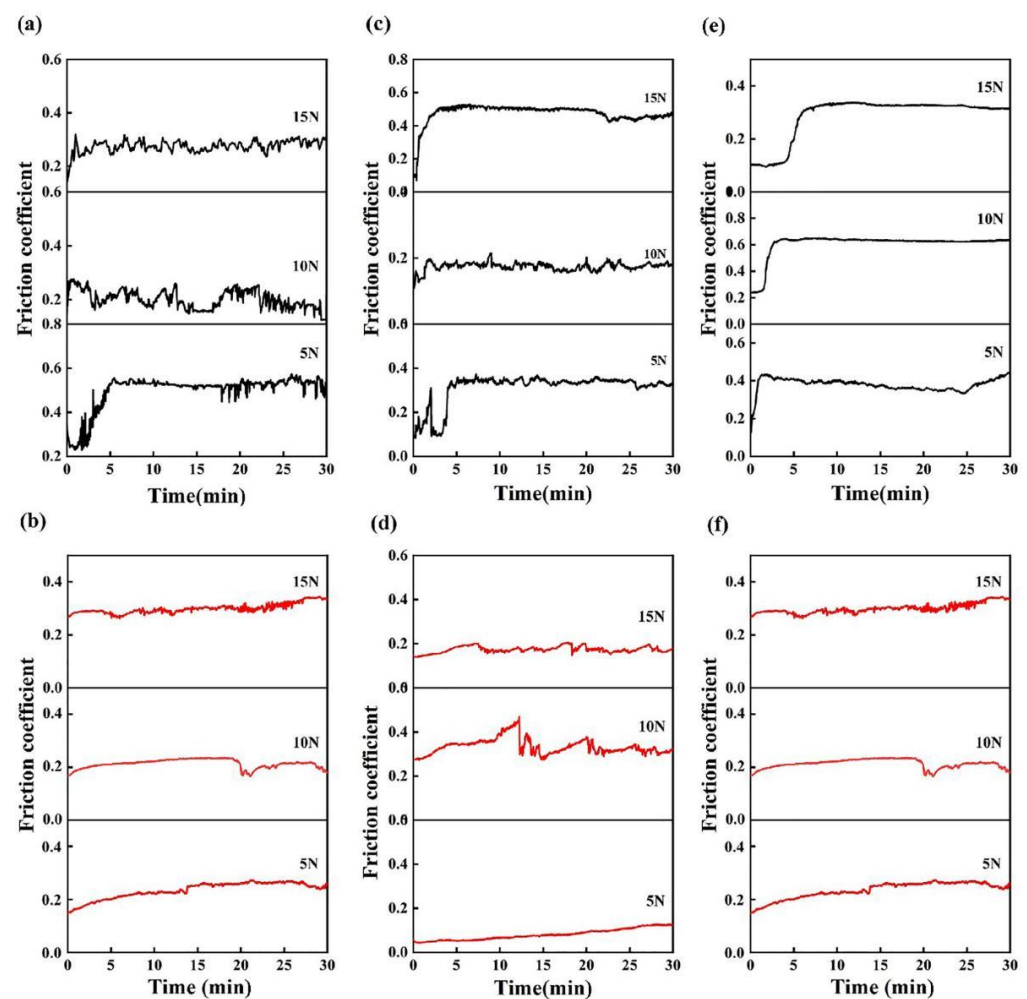


**Figure 5.** Friction coefficient as a function of the sliding time for the present HEAs: (a) hot-rolled alloy in the dry condition; (b) boronized alloy in the dry condition; (c) hot-rolled alloy in the deionized water; (d) boronized alloy in the deionized water; (e) hot-rolled alloy in the seawater; and (f) boronized alloy in the seawater.

**Table 2.** Average friction coefficient of hot-rolled and boronized Fe<sub>40</sub>Mn<sub>20</sub>Cr<sub>20</sub>Ni<sub>20</sub> HEAs under different conditions.

Average Friction Coefficient	Air			Deionized Water			Seawater		
	5 N	10 N	15 N	5 N	10 N	15 N	5 N	10 N	15 N
Hot rolled	0.50	0.20	0.38	0.31	0.37	0.18	0.38	0.61	0.55
Boronized	0.24	0.21	0.30	0.08	0.33	0.17	0.18	0.44	0.45

The friction coefficient of the hot-rolled alloys increases rapidly to 0.55 in the first 300 s and then fluctuates around 0.55 at 5 N in air as demonstrated in Figure 5a. Before 300 s, the friction coefficient increased rapidly due to the sinking of the indenter at the initial stage of friction, the low hardness and high plasticity of the hot-rolled alloy and the surface fracture and the generation of wear debris caused by the violent plowing action. The friction coefficient gradually stabilized after about 300 s due to the reduction in wear debris. The friction coefficient fluctuated around a stable value and exhibited obvious periodicity due to the separation of wear debris from the worn surface and the filling of wear debris into the cracks. The wear surface underwent a process of wear debris generation and then compaction during the entire cycle with an increase in the load. There was less fluctuation in the friction coefficient curve for the hot-rolled alloy at 5 N. The friction coefficient curve was smoother than that of the lower loads at 15 N. The friction coefficient was maintained at about 0.38 after 100 s due to the oxide films formed on the worn surface. Figure 5b exhibits the friction coefficient curve of the boronized Fe<sub>40</sub>Mn<sub>20</sub>Cr<sub>20</sub>Ni<sub>20</sub> HEAs in air. The friction coefficient curve at 5 N is smoother compared with that of the hot-rolled alloys. The friction coefficient maintains at about 0.25 after a slow increase of about 900 s. The friction coefficient greatly decreased compared with that of the hot-rolled alloys due to the greatly increased hardness of the boronized alloy. As a result, the surface resistance to the indentation of the hard Si<sub>3</sub>N<sub>4</sub> ball was improved, and the plastic deformation generated on the surface became smaller. The curve gradually stabilized after 300 s with the load increasing to 10 N. The friction coefficient drastically decreased at about 1,200 s and then increased due to the local oxide films formed on the worn surface. Then, the oxide films were torn. The curve increases slowly during the entire cycle and finally maintains at about 0.33 with the load increasing to 15 N.

Figure 5c,d show the friction coefficients of the hot-rolled and boronized HEAs in the deionized water. It can be seen that the friction coefficient reaches a stable value after 300 s at 5 N. It fluctuates up and down within 0.28. The friction coefficient greatly reduced compared with that in the dry condition due to the cleaning and lubricating by the deionized water on the worn surface. When the load is 10 N, the friction coefficient increases to 0.2 at the beginning of wear, and then the friction coefficient fluctuates around 0.2. The friction coefficient reaches the stable stage after 90 s and keeps a cyclical fluctuation at 0.16 until the slide ends with the load increasing to 15 N due to the alternant forming and eliminating of wear debris during the entire sliding process. It can be observed that the friction coefficient increases slowly, and the average friction coefficient value is 0.11 at 5 N, as shown in Figure 5d. The boronized alloy had a longer running-in period compared with that of the hot-rolled alloy in the deionized water. The average friction coefficient value is 0.33 with the load increasing to 10 N. The surface of the boronized alloy has a high roughness, resulting in the instability of the friction coefficient and severe grinding. The friction coefficient curve is smoother at 15 N. The average friction coefficient decreased. The friction coefficient gradually stabilizes above 300 s and keeps cyclical fluctuation at 0.16 until the slide ends.

The friction coefficient of the hot-rolled and boronized Fe<sub>40</sub>Mn<sub>20</sub>Cr<sub>20</sub>Ni<sub>20</sub> HEAs in the seawater under different loads is displayed in Figure 5e,f. The friction coefficient curve is smoother compared with that in other environments. The average friction coefficient of the hot-rolled alloy at 5 N, 10 N and 15 N is 0.38, 0.61 and 0.55, respectively. The friction coefficient value increased compared with that of the hot-rolled alloys in the deionized

water due to the increased roughness of the worn surface caused by the corrosion of seawater. The friction coefficient curves initially rise due to the dropping of the indenter at 5 N and then gradually decrease to a stable value owing to the cleaning and lubricating effects of seawater on the worn surface. The friction coefficient reaches a stable stage above 180 s and subsequently keeps a cyclical fluctuation at 0.65 until the slide ends with the load increasing to 10 N. The friction coefficient curve of 15 N is similar to that of 10 N. The steady state was reached after 300 s. The average friction coefficient of boronized alloys at 5 N, 10 N and 15 N is 0.18, 0.44 and 0.45, respectively. The friction coefficient rises at the initial stage and then decreases to 0.16 at 5 N. The high surface roughness of the boronized alloy initially resulted in a high friction coefficient, and then the polishing effect made the surface smoother and reduced the friction coefficient. Moreover, the corrosion of seawater softened the surface, which was easily plowed to produce wear debris. Subsequently, the wear debris was further pressed into the wear surface, and the surface became smooth, reducing the friction coefficient. The friction coefficient increases before 600 s and reaches the stable stage after 900 s with the load increasing to 10 N. As the load further increases, the friction coefficient stabilizes. This may be attributable to the polish effect, which makes the wear surface smooth.

It can be observed that the coefficient of friction in the deionized water is lower than that in dry environments and seawater due to the lubricating effect of deionized water. In contrast, the friction coefficient in the seawater is higher than that in the deionized water probably due to the corrosion effect of seawater.

### 3.3.3. Worn Surface and Wear Mechanism

Figure 6 shows the SEM images of the worn surface of the hot-rolled and boronized  $\text{Fe}_{40}\text{Mn}_{20}\text{Cr}_{20}\text{Ni}_{20}$  HEAs under different loads in air. It can be seen that there is a significant difference on the worn surface as the load increases. Cracks are observed on the worn surface of the hot-rolled  $\text{Fe}_{40}\text{Mn}_{20}\text{Cr}_{20}\text{Ni}_{20}$  HEAs at 5 N in air, as shown in Figure 6a. Moreover, much debris is also found, which is a typical feature of abrasive wear. The EDS point analysis reveals that most of the worn surfaces contain oxygen, especially the bright regions in the SEM image (Figure 6a). Therefore, the wear mechanism of the hot-rolled  $\text{Fe}_{40}\text{Mn}_{20}\text{Cr}_{20}\text{Ni}_{20}$  HEAs at 5 N in air was abrasive wear and mild oxidation wear. The hardness of the  $\text{Si}_3\text{N}_4$  ball was higher than that of the hot-rolled  $\text{Fe}_{40}\text{Mn}_{20}\text{Cr}_{20}\text{Ni}_{20}$  HEAs mainly composed of a soft FCC phase with a hardness of 139 HV, leading to abrasive wear. As the load increases, the degree of plastic deformation on the surface of the FCC alloy increases. There are wide and deep plow grooves parallel to the sliding direction and some cracks on the surface. In addition, the number of abrasive debris is reduced. The degree of plastic deformation exceeded a certain threshold during the friction process, leading to the sprouting and expansion of cracks and the spalling of materials as well as the formation of abrasive debris. Grinding debris was continuously generated and compacted on the surface during the reciprocating friction process. Therefore, the wear surface became smoother, and the friction coefficient decreased. The results are consistent with the above friction coefficient. The wear surface is severely damaged with a further increase in the load. As a result, the coefficient of friction further increased. A large number of grooves parallel to the sliding direction and broken wear debris particles adhering to the surface are observed on the wear surface in Figure 6b. The features of cracks and delamination are visible. According to the SEM images and EDS results (in Table 3), there is a certain degree of oxidation on both the wear surface and wear debris, proving the occurrence of oxidative wear. The wear surface of the alloy was continuously heated during the wear process, which raised the temperature of the local contact area of the surface and led to surface oxidation. Moreover, the EDS results show the presence of Si in the wear chips, indicating material transfer. The wear surface was damaged more severely with an increase in the load, increasing the wear rate gradually, which was consistent with the above wear rates.

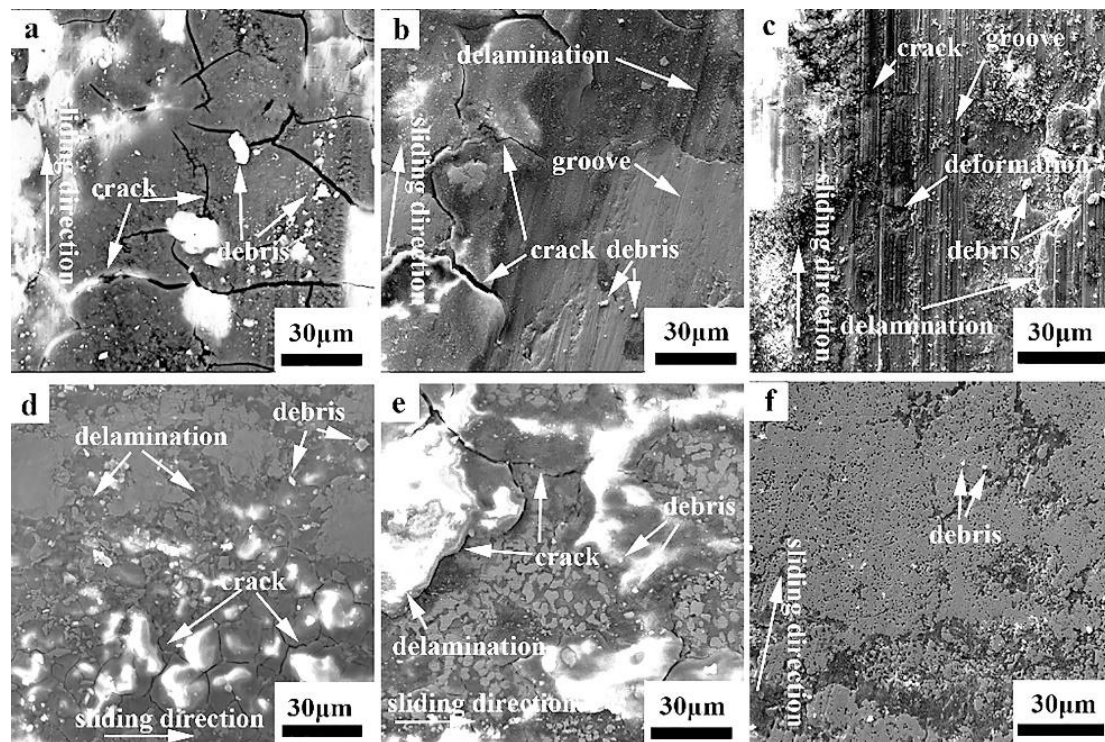


**Figure 6.** SEM images of the worn surfaces of the hot-rolled and boronized  $\text{Fe}_{40}\text{Mn}_{20}\text{Cr}_{20}\text{Ni}_{20}$  HEAs under the dry condition: (a) hot-rolled HEA, 5 N; (b) hot-rolled HEA, 10 N; (c) hot-rolled HEA, 15 N; (d) boronized HEA, 5 N; (e) boronized HEA, 10 N; and (f) boronized HEA, 15 N.

**Table 3.** EDS results of the worn surfaces and worn debris of hot-rolled and boronized  $\text{Fe}_{40}\text{Mn}_{20}\text{Cr}_{20}\text{Ni}_{20}$  HEAs under different loads in the dry environment (at. %).

Sample State	Fe	Mn	Cr	Ni	B	O	Si
Hot rolled; 5 N							
Surface	$16.7 \pm 0.1$	$3.4 \pm 0.1$	$6.1 \pm 0.1$	$10.8 \pm 0.1$	-	$63.0 \pm 0.1$	-
Debris	$25.1 \pm 0.1$	$10.4 \pm 0.1$	$11.8 \pm 0.1$	$10.9 \pm 0.1$	-	$41.8 \pm 0.1$	-
Hot rolled; 10 N							
Surface	$28.8 \pm 0.1$	$11.8 \pm 0.1$	$13.7 \pm 0.1$	$13.1 \pm 0.1$	-	$32.6 \pm 0.1$	-
Debris	$26.1 \pm 0.1$	$9.8 \pm 0.1$	$11.4 \pm 0.1$	$11.8 \pm 0.1$	-	$39.8 \pm 0.1$	$1.1 \pm 0.1$
Hot rolled; 15 N							
Surface	$24.4 \pm 0.1$	$11.8 \pm 0.1$	$15.7 \pm 0.1$	$11.9 \pm 0.1$	-	$36.2 \pm 0.1$	-
Debris	$18.9 \pm 0.1$	$7.9 \pm 0.1$	$8.8 \pm 0.1$	$7.6 \pm 0.1$	-	$54.3 \pm 0.1$	$2.5 \pm 0.1$
Boronized; 5 N							
Surface	$29.1 \pm 0.1$	$10.0 \pm 0.1$	$18.9 \pm 0.1$	$7.5 \pm 0.1$	$14.3 \pm 0.1$	$20.2 \pm 0.1$	-
Debris	$25.2 \pm 0.1$	$8.3 \pm 0.1$	$13.8 \pm 0.1$	$4.1 \pm 0.1$	$1.7 \pm 0.1$	$45.2 \pm 0.1$	$1.7 \pm 0.1$
Boronized; 10 N							
Surface	$22.4 \pm 0.1$	$11.6 \pm 0.1$	$14.2 \pm 0.1$	$12.2 \pm 0.1$	$17.1 \pm 0.1$	$20.5 \pm 0.1$	$2.0 \pm 0.1$
Debris	$18.4 \pm 0.1$	$6.5 \pm 0.1$	$7.5 \pm 0.1$	$7.3 \pm 0.1$	$3.5 \pm 0.1$	$50.9 \pm 0.1$	$5.9 \pm 0.1$
Boronized; 15 N							
Surface	$29.7 \pm 0.1$	$13.2 \pm 0.1$	$15.2 \pm 0.1$	$13.6 \pm 0.1$	$14.9 \pm 0.1$	$10.2 \pm 0.1$	$3.2 \pm 0.1$
Debris	$20.7 \pm 0.1$	$8.9 \pm 0.1$	$9.2 \pm 0.1$	$8.7 \pm 0.1$	$5.3 \pm 0.1$	$44.6 \pm 0.1$	$2.6 \pm 0.1$

The SEM images of the worn surface of the boronized  $\text{Fe}_{40}\text{Mn}_{20}\text{Cr}_{20}\text{Ni}_{20}$  HEAs under different loads in air are presented in Figure 6d–f. It can be seen that many cracks, some debris and delamination features are found on the worn surface at 5 N due to the brittleness of the boride layer, as shown in Figure 6d. The wear surface morphologies of the boronized

Fe<sub>40</sub>Mn<sub>20</sub>Cr<sub>20</sub>Ni<sub>20</sub> HEAs at 10 N are similar to those at 5 N. The cracks, wear debris and delamination appeared on the worn surface, showing the characteristics of delamination wear. Some grooves are observed and no cracks can be detected in Figure 6f. The wear surface was not destroyed, and the wear mechanism was the polishing effect. When the load increased, the cracks expanded, and the material surface was peeled off to form abrasive debris, which was further compacted on the surface, reducing the friction coefficient. At this time, the friction was still in the grinding stage. In the whole friction process, the worn surface gradually became smooth, and the contact stress between the substrate and the Si<sub>3</sub>N<sub>4</sub> ball was reduced and then entered the stable period. The wear rate increased due to the flaking of the alloy on the wear surface with increasing the load from 5 N to 10 N. The wear surface was in high engagement with the friction substrate with increasing the load to 15 N, decreasing the wear rate. This was consistent with the above wear rates.

The worn surface morphology of the hot-rolled and boronized Fe<sub>40</sub>Mn<sub>20</sub>Cr<sub>20</sub>Ni<sub>20</sub> HEAs under different loads in the deionized water is presented in Figure 7. The wear debris on the worn surface was less than that in the dry condition. The local stress, heat concentration and shear friction were reduced in the liquid environment, thereby inhibiting the generation of cracks. More grooves parallel to the sliding direction and some debris are observed on the worn surface, as shown in Figure 7a, which is a typical feature of abrasive wear. The wide and deep furrows were easily produced when the small Si<sub>3</sub>N<sub>4</sub> balls were pressed into the surface of the alloy due to the high plasticity of FCC alloys. As shown in Figure 7b, a large number of grooves parallel to the sliding direction and some cracks are observed on the worn surface with the load increasing to 10 N due to the increase in the degree of plastic deformation of the alloy and the sprouting and expansion of cracks in the subsurface of the alloy. Moreover, the number of debris was significantly reduced, and there was a dark area. The wear surface became rougher, increasing the friction coefficient and wear rate. It was implied that the wear mechanism was abrasive wear and delamination wear. In Figure 7c, deeper and wider grooves parallel to the sliding direction are observed with a further increase in the load, suggesting a mechanism of abrasive wear. Furthermore, some cracks are discovered on the worn surface, indicating that delamination wear occurred. The EDS analysis reveals that the worn surface contains oxygen, as shown in Table 4. On the one hand, the frictional heat was greatly reduced due to the cooling effect of the liquid. On the other hand, the deionized water insulated the oxygen and reduced the oxidation of the worn surface. However, mild oxidation was inevitable. Additionally, the wear rate in the deionized water was higher than that in the dry condition due to the lack of a large area of oxide film in the deionized water. Moreover, there was a transfer of materials when the load was 10 N. The flaking of the Si<sub>3</sub>N<sub>4</sub> spheres generated abrasive debris, part of which was cleaned by the deionized water and the other part was compacted on the surface, forming a mechanical mixed layer, playing the role of lubrication and reducing the wear rate.

Figure 7d–f show the SEM micrograph of the wear surface of the boronized Fe<sub>40</sub>Mn<sub>20</sub>Cr<sub>20</sub>Ni<sub>20</sub> HEAs at different loads in the deionized water. It can be seen that the wear morphology under different loads is similar. Many grooves parallel to the sliding direction and a small amount of wear debris are found on the worn surface, suggesting the wear mechanism of abrasive wear. Moreover, many cracks appeared due to the brittle surface. This is characteristic of delamination wear. The amount of abrasive debris on the surface is greatly reduced in the deionized water compared to that in the dry environment due to the cleaning and lubricating effect of deionized water. The plowing effect of the Si<sub>3</sub>N<sub>4</sub> spheres on the alloy surface resulted in a more severe spalling of the wear surface and an increase in the wear rate with an increase in the load. This was consistent with the wear rate results. The increased load increases the contact area between the alloy and the friction substrate, which facilitates the compaction of the abrasive chips. This leads to a lower wear rate. The grooves on the worn surface decrease and the cracks increase with the load increasing to 15 N. Therefore, the predominant wear mechanism was transformed from abrasive wear to delamination wear. In combination with the EDS results, the presence of large amounts

of oxygen on the wear surface indicates the occurrence of oxidative wear. Moreover, the presence of Si is detected on the wear surface at 5 N and 10 N, indicating material transfer. Si is transferred to the wear surface, forming a mechanically mixed layer, which acts as a lubricant.

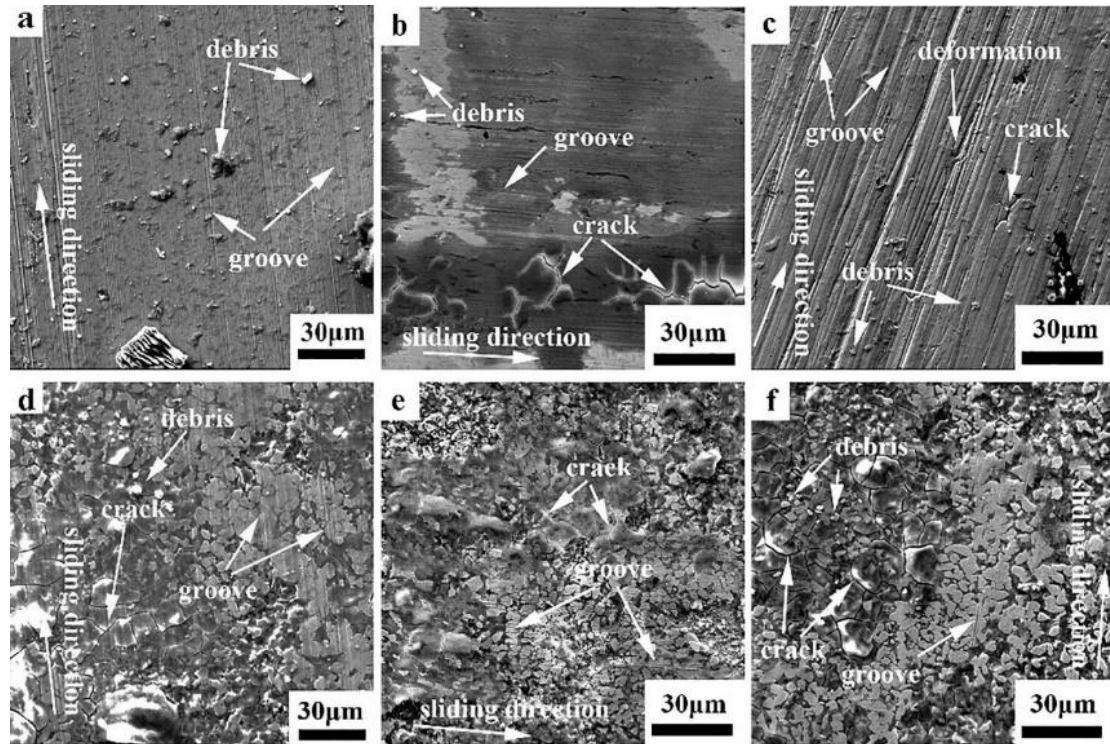


**Figure 7.** SEM images of the worn surfaces of the hot-rolled and boronized  $\text{Fe}_{40}\text{Mn}_{20}\text{Cr}_{20}\text{Ni}_{20}$  HEAs in the deionized water: (a) hot-rolled HEA, 5 N; (b) hot-rolled HEA, 10 N; (c) hot-rolled HEA, 15 N; (d) boronized HEA, 5 N; (e) boronized HEA, 10 N; and (f) boronized HEA, 15 N.

**Table 4.** EDS results of the worn surfaces and worn debris of hot-rolled and boronized  $\text{Fe}_{40}\text{Mn}_{20}\text{Cr}_{20}\text{Ni}_{20}$  HEAs under different loads in the deionized water (at. %).

Sample State	Fe	Mn	Cr	Ni	B	O	Si
Hot Rolled; 5 N							
Surface	$33.4 \pm 0.1$	$13.4 \pm 0.1$	$15.7 \pm 0.1$	$14.5 \pm 0.1$	-	$23.0 \pm 0.1$	-
Debris	$22.6 \pm 0.1$	$12.1 \pm 0.1$	$10.3 \pm 0.1$	$14.4 \pm 0.1$	-	$25.9 \pm 0.1$	$14.7 \pm 0.1$
Hot rolled; 10 N							
Surface	$26.6 \pm 0.1$	$10.7 \pm 0.1$	$12.5 \pm 0.1$	$11.9 \pm 0.1$	-	$35.9 \pm 0.1$	$2.4 \pm 0.1$
Debris	$25.1 \pm 0.1$	$9.9 \pm 0.1$	$11.7 \pm 0.1$	$11.2 \pm 0.1$	-	$39.3 \pm 0.1$	$2.8 \pm 0.1$
Hot rolled; 15 N							
Surface	$32.7 \pm 0.1$	$13.4 \pm 0.1$	$15.7 \pm 0.1$	$15.1 \pm 0.1$	-	$23.1 \pm 0.1$	-
Debris	$38.7 \pm 0.1$	$15.9 \pm 0.1$	$18.5 \pm 0.1$	$17.8 \pm 0.1$	-	$9.1 \pm 0.1$	-
Boronized; 5 N							
Surface	$13.3 \pm 0.1$	$5.1 \pm 0.1$	$0.4 \pm 0.1$	$17.0 \pm 0.1$	$11.7 \pm 0.1$	$35.4 \pm 0.1$	$17.1 \pm 0.1$
Debris	$11.7 \pm 0.1$	$6.2 \pm 0.1$	$8.2 \pm 0.1$	$53.1 \pm 0.1$	$3.5 \pm 0.1$	$15.6 \pm 0.1$	$1.7 \pm 0.1$
Boronized; 10 N							
Surface	$16.5 \pm 0.1$	$8.3 \pm 0.1$	$5.7 \pm 0.1$	$7.5 \pm 0.1$	$15.2 \pm 0.1$	$31.4 \pm 0.1$	$15.4 \pm 0.1$
Debris	$5.6 \pm 0.1$	$5.7 \pm 0.1$	$7.6 \pm 0.1$	$4.8 \pm 0.1$	$5.6 \pm 0.1$	$68.2 \pm 0.1$	$2.5 \pm 0.1$
Boronized; 15 N							
Surface	$13.1 \pm 0.1$	$2.7 \pm 0.1$	$5.4 \pm 0.1$	$16.2 \pm 0.1$	$12.2 \pm 0.1$	$50.4 \pm 0.1$	-
Debris	$4.4 \pm 0.1$	$3.9 \pm 0.1$	$0.4 \pm 0.1$	$66.4 \pm 0.1$	$4.4 \pm 0.1$	$20.5 \pm 0.1$	-

Figure 8 shows the SEM images of the wear surface of the hot-rolled and boronized  $\text{Fe}_{40}\text{Mn}_{20}\text{Cr}_{20}\text{Ni}_{20}$  HEAs under different loads in the simulated seawater. As illustrated in Figure 8a, a great number of grooves densely appear on the worn surface and some wear debris is randomly distributed on the surface at 5 N, suggesting the wear mechanism of abrasive wear. According to the EDS results, the worn surface contains a lot of oxygen, which indicates that a protective passivation film was formed in the seawater to block the attack of chloride ions. Therefore, the wear rate was lower. When the load increases to 10 N, as displayed in Figure 8b, more grooves on the wear surface appear and are deeper, and there is more abrasive debris due to the corrosive effect of seawater, which makes the wear surface looser and softer. The degree of plastic deformation of the wear surface increased with an increase in the load, which led to the flaking of the materials and the formation of abrasive debris when the threshold value was exceeded. Moreover, the passivation film was destroyed more easily with an increase in the load, exposing a new metal surface and increasing the corrosion and wear. The wear surface became rougher, increasing the friction coefficient and wear rate. As illustrated in Figure 8c, when the load increases to 15 N, in addition to the presence of a large number of grooves and abrasive debris, cracks appear. The wear mechanism changed to abrasive wear and delamination wear. The wear surface was severely damaged, and the wear rate increased further. The EDS results (in Table 5) indicate the presence of Na and Cl on the wear surface, indicating that the wear surface was subjected to corrosion caused by the seawater. Therefore, the wear rate in the seawater was higher than that in the deionized water.

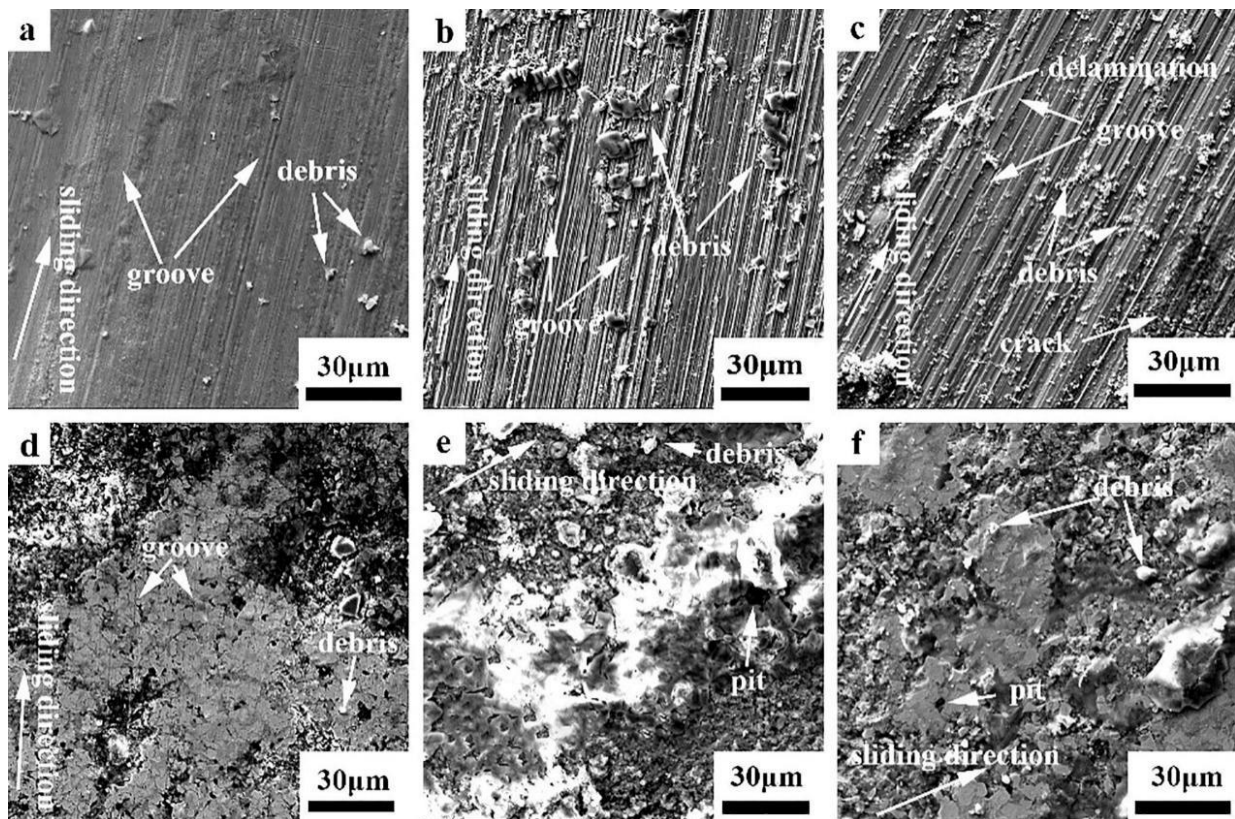


**Figure 8.** SEM images of the worn surfaces of the hot-rolled and boronized  $\text{Fe}_{40}\text{Mn}_{20}\text{Cr}_{20}\text{Ni}_{20}$  HEAs in the seawater: (a) hot-rolled HEA, 5 N; (b) hot-rolled HEA, 10 N; (c) hot-rolled HEA, 15 N; (d) boronized HEA, 5 N; (e) boronized HEA, 10 N; and (f) boronized HEA, 15 N.

**Table 5.** EDS results of the worn surfaces and worn debris of hot-rolled and boronized Fe<sub>40</sub>Mn<sub>20</sub>Cr<sub>20</sub>Ni<sub>20</sub> HEAs under different loads in the seawater (at. %).

Sample State	Fe	Mn	Cr	Ni	B	O	Na	Cl
Hot rolled; 5 N								
Surface	19.3 ± 0.1	7.2 ± 0.1	9.9 ± 0.1	8.8 ± 0.1	-	42.4 ± 0.1	8.7 ± 0.1	3.7 ± 0.1
Debris	4.2 ± 0.1	1.1 ± 0.1	1.8 ± 0.1	1.0 ± 0.1	-	15.4 ± 0.1	54.8 ± 0.1	21.7 ± 0.1
Hot rolled; 10 N								
Surface	29.4 ± 0.1	14.9 ± 0.1	13.3 ± 0.1	13.6 ± 0.1	-	28.8 ± 0.1	-	-
Debris	9.0 ± 0.1	2.8 ± 0.1	3.7 ± 0.1	2.9 ± 0.1	-	2.4 ± 0.1	60.2 ± 0.1	19.0 ± 0.1
Hot rolled; 15 N								
Surface	32.1 ± 0.1	13.0 ± 0.1	15.2 ± 0.1	14.7 ± 0.1	-	24.9 ± 0.1	-	0.1 ± 0.1
Debris	26.9 ± 0.1	9.7 ± 0.1	13.9 ± 0.1	12.2 ± 0.1	-	35.2 ± 0.1	0.4 ± 0.1	1.7 ± 0.1
Boronized; 5 N								
Surface	10.2 ± 0.1	6.5 ± 0.1	4.6 ± 0.1	12.4 ± 0.1	6.4 ± 0.1	26.9 ± 0.1	20.3 ± 0.1	12.7 ± 0.1
Debris	7.3 ± 0.1	7.5 ± 0.1	4.5 ± 0.1	17.6 ± 0.1	8.4 ± 0.1	40.2 ± 0.1	12.6 ± 0.1	1.8 ± 0.1
Boronized; 10 N								
Surface	13.6 ± 0.1	1.1 ± 0.1	1.5 ± 0.1	10.6 ± 0.1	19.4 ± 0.1	24.2 ± 0.1	24.2 ± 0.1	5.4 ± 0.1
Debris	9.8 ± 0.1	1.6 ± 0.1	1.5 ± 0.1	7.8 ± 0.1	18.5 ± 0.1	28.4 ± 0.1	28.3 ± 0.1	4.1 ± 0.1
Boronized; 15 N								
Surface	7.3 ± 0.1	5.4 ± 0.1	0.3 ± 0.1	74.2 ± 0.1	4.4 ± 0.1	4.3 ± 0.1	2.6 ± 0.1	0.9 ± 0.1
Debris	4.5 ± 0.1	40.5 ± 0.1	0.7 ± 0.1	13.0 ± 0.1	5.2 ± 0.1	36.1 ± 0.1	-	-

The SEM images of the wear surface of the boronized Fe<sub>40</sub>Mn<sub>20</sub>Cr<sub>20</sub>Ni<sub>20</sub> HEAs are displayed in Figure 8d–f. At a low load, many shallow grooves exist on the wear surface. Due to the polishing effect, the wear surface becomes smoother. Therefore, the coefficient of friction and the wear rate were lower. The wear mechanism was abrasive wear. The alloy surface becomes looser owing to the corrosive effect of seawater. The degree of plastic deformation increases with an increase in the load, resulting in the peeling off of the material surface. The alloy surface becomes rougher, and the friction coefficient increases, which is consistent with the friction coefficient results. Some wear debris and pits are observed on the worn surface with an increase in the load, indicating that the wear mechanism was abrasive wear and corrosion wear with the load increasing to 15 N. The wear surface underwent a cyclic process of abrasive debris shedding and compaction decreasing the wear rate. Based on the wear morphology, the occurrence of oxidative wear can be judged. Combined with the EDS results, oxidative wear was further demonstrated. After boronizing, Fe<sub>2</sub>B exists on the surface. Compared with Fe in the matrix, it was hard for Fe<sub>2</sub>B to lose electrons, and it had better chemical stability, improving its corrosion resistance to a certain extent. Therefore, the wear rate of the boronized alloy in the seawater was lower than that of the hot-rolled alloy.

### 3.4. XPS Examination

The XPS analysis of the worn surface of the boronized HEA in the seawater at 15 N is displayed in Figure 9. During the reciprocating sliding process, a large amount of frictional heat was generated at the contact interface, leading to oxidation of the worn surface and the formation of metal oxides. Figure 9a shows the full spectrum of the sample. It can be clearly seen that there are peaks of Fe, Mn, Cr, Ni, O, B and Cl. According to Figure 9b,e, there are a large number of metal oxides and hydroxides on the wear surface, including FeO, Fe<sub>2</sub>O<sub>3</sub>, Mn<sub>3</sub>O<sub>4</sub>, MnO<sub>2</sub>, Cr<sub>2</sub>O<sub>3</sub> and Ni(OH)<sub>2</sub>. The existence of the oxide film prevented the direct contact of the friction pairs and reduced the wear rate. At the same time, according to Figure 9g, BN and B<sub>2</sub>O<sub>3</sub> were detected on the worn surface, proving that the borides on the worn surface chemically reacted with the Si<sub>3</sub>N<sub>4</sub> of the friction pair. B<sub>2</sub>O<sub>3</sub> reacted with water to form boric acid [35,36], which had a lubricating effect. However, the boric acid easily decomposed, which was not shown in XPS. BN has a lubricating effect, thus reducing the

wear rate and improving wear resistance. According to Figure 9h, chlorides were detected, which was caused by the small radius of chloride ions and the high solubility of chlorides. The chloride ions easily entered and destroyed the oxide film, aggravating the wear. In addition, according to Figure 9f,  $\text{SiO}_2$  is detected on the worn surface, which is caused by the oxidation of  $\text{Si}_3\text{N}_4$  in the seawater. The reaction of  $\text{SiO}_2$  and  $\text{H}_2\text{O}$  can also generate  $\text{SiO}_2 \cdot n\text{H}_2\text{O}$  and  $\text{Si}(\text{OH})_4$ , which have a lubricating effect. The chemical reactions involved above are as follows [37–39]:

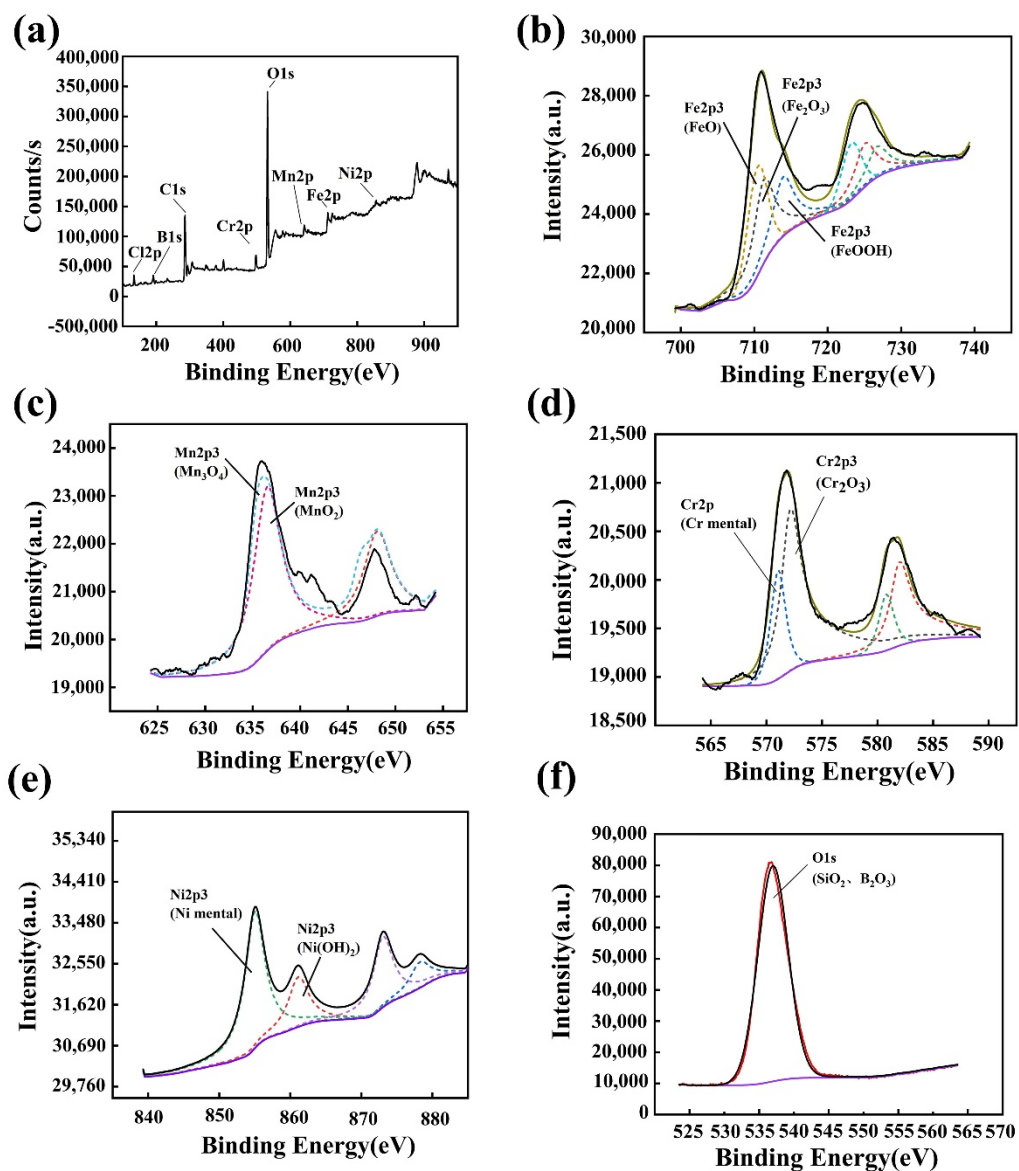
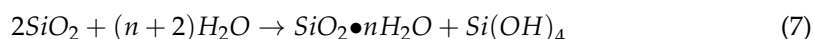
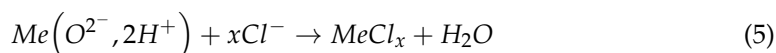
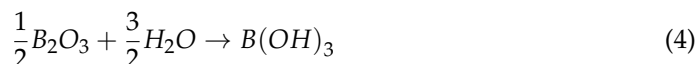
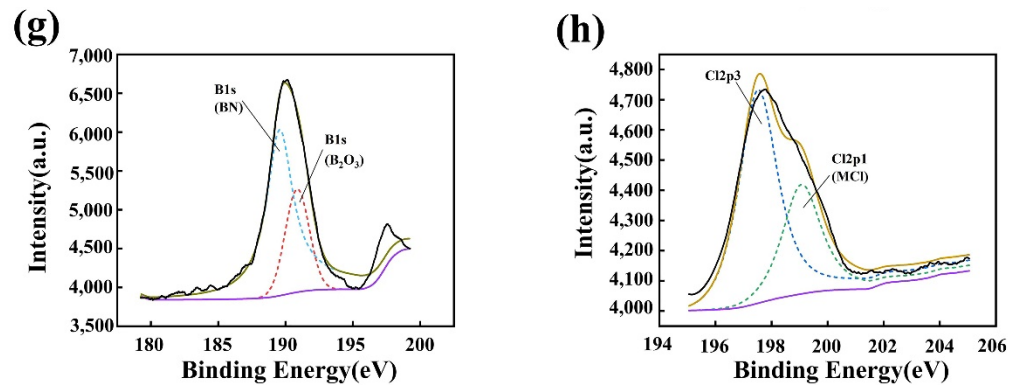


Figure 9. Cont.



**Figure 9.** XPS analysis of the worn surface of the boronized HEA in the seawater at 15 N. (a) Full spectrum of the sample (b) Fe element; (c) Mn element; (d) Cr element; (e) Ni element; (f) O element; (g) B element; (h) Cl element.

Thus, the low wear rate of the boronized HEA was caused by the synergistic effect of boric acid,  $\text{SiO}_2 \cdot n\text{H}_2\text{O}$  and  $\text{Si}(\text{OH})_4$ . The boric acid had a lubricating effect. In addition, the existence of oxide film prevented direct contact between the friction pair and the alloy.

#### 4. Conclusions

In the present study, a boronized layer was prepared on the surface of  $\text{Fe}_{40}\text{Mn}_{20}\text{Cr}_{20}\text{Ni}_{20}$  HEAs using solid boron leakage technology. The microstructure and tribological properties of hot-rolled and boronized alloys were studied. The following conclusions could be drawn:

(1) The hot-rolled alloy only consisted of the FCC phase. The surface after boronizing was composed of many borides, including  $\text{CrB}$ ,  $\text{FeB}$ ,  $\text{MnB}$ ,  $\text{Fe}_2\text{B}$ ,  $\text{Fe}_3\text{B}$ ,  $\text{MnB}_2$ ,  $\text{BNi}_3$ ,  $\text{Cr}_5\text{B}_3$ ,  $\text{Cr}_2\text{B}_3$  and  $\text{Ni}_4\text{B}_3$ . The cross-section of the boronized alloy presented a layered structure, which can be divided into the boride layer, the diffusion layer and the matrix. The thickness of the boride layer was  $50.2 \mu\text{m}$ . The hardness of the alloy increased from 139 HV to 970 HV after boronizing.

(2) The wear rate of the boronized alloy was lower than that of the hot-rolled alloy, especially in the seawater. In the air, the wear rate of the hot-rolled alloy gradually increased with an increase in the load. However, the wear rate of the boronized alloy first increased and then decreased. In the deionized water, both the wear rates of hot-rolled and boronized alloys first increased and then decreased with an increase in the load. In the seawater, the wear rate of the hot-rolled alloy increased with an increase in the load. Nevertheless, the wear rate of the boronized alloy first increased and then decreased with an increase in the load.

(3) In the dry environment, the wear mechanism of the hot-rolled alloy was abrasive wear and oxidation wear at a low load, which changed to abrasive wear, delamination wear and oxidative wear with an increase in the load. The wear mechanism of the boronized alloy was delamination wear and oxidation wear at a low load, which changed to the polishing effect and oxidation wear with the load increasing to 15 N.

(4) In the deionized water, the wear mechanism of the hot-rolled alloy was abrasive wear at a low load, which changed to abrasive wear and delamination wear with an increase in the load. In contrast, the wear mechanism of the boronized alloy was abrasive wear, delamination wear and oxidative wear.

(5) In the seawater, the wear mechanism of the hot-rolled alloy was abrasive wear and corrosive wear at low loads, which changed to abrasive wear, delamination wear and corrosive wear with the load increasing to 15 N. The wear mechanism of the boronized alloys was abrasive wear, corrosion wear and oxidation wear.

**Author Contributions:** Writing, X.G.; literature search, X.J.; figures and study design, X.S.; data collection, H.Y.; data analysis, M.Z.; data interpretation: J.Q. All authors have read and agreed to the published version of the manuscript.

**Funding:** The authors would like to acknowledge the financial support of the Natural Science Foundation of Shanxi Province, China (Nos. 201901D111105 and 201901D111114), Transformation of Scientific and Technological Achievements Programs of Higher Education Institutions in Shanxi (2019), and the opening project of State Key Laboratory of Explosion Science and Technology (Beijing Institute of Technology), and the opening project number is KFJJ20-13M.

**Institutional Review Board Statement:** Not applicable.

**Informed Consent Statement:** Informed consent was obtained from all subjects involved in the study.

**Data Availability Statement:** Not applicable.

**Conflicts of Interest:** This article is original. The article has been written by the stated authors that are all aware of its content and approve its submission. The article has not been published previously. The article is not under consideration for publication elsewhere. No conflict of interest exists, or if such conflict exists, the exact nature must be declared. If accepted, the article will not be published elsewhere in the same form, in any language, without the written consent of the publisher.

## References

1. Yeh, J.-W.; Chen, S.-K.; Lin, S.-J.; Gan, J.-Y.; Chin, T.-S.; Shun, T.-T.; Tsau, C.-H.; Chang, S.-Y. Nanostructured high-entropy alloys with multiple principal elements: Novel alloy design concepts and outcomes. *Adv. Eng. Mater.* **2004**, *6*, 299–303. [[CrossRef](#)]
2. Miracle, D.; Senkov, O. A critical review of high entropy alloys and related concepts. *Acta Mater.* **2017**, *122*, 448–511. [[CrossRef](#)]
3. He, J.; Liu, W.; Wang, H.; Wu, Y.; Liu, X.; Nieh, T.; Lu, Z. Effects of Al addition on structural evolution and tensile properties of the FeCoNiCrMn high-entropy alloy system. *Acta Mater.* **2014**, *62*, 105–113. [[CrossRef](#)]
4. Stepanov, N.; Yurchenko, N.; Skibin, D.; Tikhonovsky, M.; Salishchev, G. Structure and mechanical properties of the AlCr<sub>x</sub>NbTiV (x = 0, 0.5, 1, 1.5) high entropy alloys. *J. Alloys Compd.* **2015**, *652*, 266–280. [[CrossRef](#)]
5. Tsai, M.-H.; Yeh, J.-W. High-entropy alloys: A critical review. *Mater. Res. Lett.* **2014**, *2*, 107–123. [[CrossRef](#)]
6. Yang, X.; Zhang, Y. Prediction of high-entropy stabilized solid-solution in multi-component alloys. *Mater. Chem. Phys.* **2012**, *132*, 233–238. [[CrossRef](#)]
7. Zhang, Y.; Yang, X.; Liaw, P.K. Alloy design and properties optimization of high-entropy alloys. *JOM* **2012**, *64*, 830–838. [[CrossRef](#)]
8. Zhang, K.; Fu, Z.; Zhang, J.; Wang, W.; Wang, H.; Wang, Y.; Zhang, Q.; Shi, J. Microstructure and mechanical properties of CoCrFeNiTiAl<sub>x</sub> high-entropy alloys. *Mater. Sci. Eng. A* **2009**, *508*, 214–219. [[CrossRef](#)]
9. Ma, S.; Zhang, Y. Effect of Nb addition on the microstructure and properties of AlCoCrFeNi high-entropy alloy. *Mater. Sci. Eng. A* **2012**, *532*, 480–486. [[CrossRef](#)]
10. Otto, F.; Dlouhý, A.; Somsen, C.; Bei, H.; Eggeler, G.; George, E. The influences of temperature and microstructure on the tensile properties of a CoCrFeMnNi high-entropy alloy. *Acta Mater.* **2013**, *61*, 5743–5755. [[CrossRef](#)]
11. Tong, C.-J.; Chen, M.-R.; Yeh, J.-W.; Lin, S.-J.; Chen, S.-K.; Shun, T.-T.; Chang, S.-Y. Mechanical performance of the Al<sub>x</sub>CoCrCuFeNi high-entropy alloy system with multiprincipal elements. *Metall. Mater. Trans. A* **2005**, *36*, 1263–1271. [[CrossRef](#)]
12. Chuang, M.-H.; Tsai, M.-H.; Wang, W.-R.; Lin, S.-J.; Yeh, J.-W. Microstructure and wear behavior of Al<sub>x</sub>Co<sub>1.5</sub>CrFeNi<sub>1.5</sub>Ti<sub>y</sub> high-entropy alloys. *Acta Mater.* **2011**, *59*, 6308–6317. [[CrossRef](#)]
13. Qiu, X.-W.; Zhang, Y.-P.; He, L.; Liu, C.-G. Microstructure and corrosion resistance of AlCrFeCuCo high entropy alloy. *J. Alloys Compd.* **2013**, *549*, 195–199. [[CrossRef](#)]
14. Zhou, Y.J.; Zhang, A.; Wang, Y.L.; Chen, G.L. Solid solution alloys of AlCoCrFeNiTi<sub>x</sub> with excellent room-temperature mechanical properties. *Appl. Phys. Lett.* **2007**, *90*, 181904. [[CrossRef](#)]
15. Lin, C.-M.; Tsai, H.-L. Evolution of microstructure, hardness, and corrosion properties of high-entropy Al<sub>0.5</sub>CoCrFeNi alloy. *Intermetallics* **2011**, *19*, 288–294. [[CrossRef](#)]
16. Stott, F.H. The role of oxidation in the wear of alloys. *Tribol. Int.* **1998**, *31*, 61–71. [[CrossRef](#)]
17. Katsamas, A.; Haidemenopoulos, G. Laser-beam carburizing of low-alloy steels. *Surf. Coat. Technol.* **2001**, *139*, 183–191. [[CrossRef](#)]
18. Tang, W.-Y.; Yeh, J.-W. Effect of aluminum content on plasma-nitrided Al<sub>x</sub>CoCrCuFeNi high-entropy alloys. *Met. Mater. Trans. A* **2009**, *40*, 1479–1486. [[CrossRef](#)]
19. Béjar, M.; Moreno, E. Abrasive wear resistance of boronized carbon and low-alloy steels. *J. Mater. Process. Technol.* **2006**, *173*, 352–358. [[CrossRef](#)]
20. Samy, B.; Narayanan, T.S.; Ravichandran, K.S.; Park, I.S.; Lee, M.H. Pack boronizing of AISI H11 tool steel: Role of surface mechanical attrition treatment. *Vacuum* **2013**, *97*, 36–43. [[CrossRef](#)]

21. Kaczmarek, M.; Jurczyk, M.; Miklaszewski, A.; Paszel-Jaworska, A.; Romaniuk-Drapała, A.; Lipińska, N.; Żurawski, J.; Urbaniak, P.; Jurczyk, K. In vitro biocompatibility of titanium after plasma surface alloying with boron. *Mater. Sci. Eng. C* **2016**, *69*, 1240–1247. [[CrossRef](#)] [[PubMed](#)]
22. Tabur, M.; Izciler, M.; Gul, F.; Karacan, I. Abrasive wear behavior of boronized AISI 8620 steel. *Wear* **2009**, *266*, 1106–1112. [[CrossRef](#)]
23. Hou, J.; Zhang, M.; Yang, H.; Qiao, J.; Wu, Y. Surface strengthening in Al<sub>0.25</sub>CoCrFeNi high-entropy alloy by boronizing. *Mater. Lett.* **2019**, *238*, 258–260. [[CrossRef](#)]
24. Wu, Y.; Yang, H.; Guo, R.; Wang, X.; Shi, X.; Liaw, P.; Qiao, J. Tribological behavior of boronized Al<sub>0.1</sub>CoCrFeNi high-entropy alloys under dry and lubricated conditions. *Wear* **2020**, *460–461*, 203452. [[CrossRef](#)]
25. Bian, B.; Guo, N.; Yang, H.; Guo, R.; Yang, L.; Wu, Y.; Qiao, J. A novel cobalt-free FeMnCrNi medium-entropy alloy with exceptional yield strength and ductility at cryogenic temperature. *J. Alloys Compd.* **2020**, *827*, 153981. [[CrossRef](#)]
26. Nutor, R.K.; Azeemullah, M.; Cao, Q.P.; Wang, X.D.; Zhang, D.X.; Jiang, J.Z. Microstructure and properties of a Co-free Fe<sub>50</sub>Mn<sub>27</sub>Ni<sub>10</sub>Cr<sub>13</sub> high entropy alloy. *J. Alloys Compd.* **2021**, *851*, 156842. [[CrossRef](#)]
27. Meric, C.; Sahin, S.; Backir, B.; Koksall, N. Investigation of the boronizing effect on the abrasive wear behavior in cast irons. *Mater. Des.* **2006**, *27*, 751–757. [[CrossRef](#)]
28. Martini, C.; Palombarini, G.; Carbucicchio, M. Mechanism of thermochemical growth of iron borides on iron. *J. Mater. Sci.* **2004**, *39*, 933–937. [[CrossRef](#)]
29. D'Souza, B.; Leong, A.; Yang, Q.; Zhang, J. Corrosion behavior of boronized nickel-based alloys in the molten chloride salt. *Corros. Sci.* **2021**, *182*, 109285. [[CrossRef](#)]
30. Zhang, H.; Zhong, X.C.; He, Y.Z.; Li, W.H.; Wu, W.F.; Chen, G.; Guo, S. Effect of high configuration entropy and rare earth addition on boride precipitation and mechanical properties of multi-principal-element alloys. *J. Mater. Eng. Perform.* **2017**, *26*, 3750–3755. [[CrossRef](#)]
31. Zhang, H.; He, Y.; Pan, Y. Enhanced hardness and fracture toughness of the laser-solidified FeCoNiCrCuTiMoAlSiB<sub>0.5</sub> high-entropy alloy by martensite strengthening. *Scr. Mater.* **2013**, *69*, 342–345. [[CrossRef](#)]
32. Khrushchov, M. Principles of abrasive wear. *Wear* **1974**, *28*, 69–88. [[CrossRef](#)]
33. Wang, X.; Li, D. Investigation of the synergism of wear and corrosion using an electrochemical scratch technique. *Tribol. Lett.* **2001**, *11*, 117–120. [[CrossRef](#)]
34. Wu, J.-M.; Lin, S.-J.; Yeh, J.-W.; Chen, S.-K.; Huang, Y.-S.; Chen, H.-C. Adhesive wear behavior of Al<sub>x</sub>CoCrCuFeNi high-entropy alloys as a function of aluminum content. *Wear* **2006**, *261*, 513–519. [[CrossRef](#)]
35. Erdemir, A.; Bindal, C.; Fenske, G.R. Formation of ultralow friction surface films on boron carbide. *Appl. Phys. Lett.* **1996**, *68*, 1637–1639. [[CrossRef](#)]
36. Bindal, C.; Erdemir, A. Ultralow friction behavior of borided steel surfaces after flash annealing. *Appl. Phys. Lett.* **1996**, *68*, 923–925. [[CrossRef](#)]
37. Lin, X.; Bai, Z.; Liu, Y.; Tang, B.; Yang, H. Sliding tribological characteristics of in-situ dendrite-reinforced Zr-based metallic glass matrix composites in the acid rain. *J. Alloys Compd.* **2016**, *686*, 866–873. [[CrossRef](#)]
38. Xu, J.; Kato, K. Formation of tribochemical layer of ceramics sliding in water and its role for low friction. *Wear* **2000**, *245*, 61–75. [[CrossRef](#)]
39. Duan, H.; Wu, Y.; Hua, M.; Yuan, C.; Wang, D.; Tu, J.; Kou, H.; Li, J. Tribological properties of AlCoCrFeNiCu high-entropy alloy in hydrogen peroxide solution and in oil lubricant. *Wear* **2012**, *297*, 1045–1051. [[CrossRef](#)]